Recrystallization and phase transitions in a γ-TiAl-based alloy as observed by ex situ and in situ high-energy X-ray diffraction

Klaus-Dieter Liss [a,e,*], Arno Bartels [a], Helmut Clemens [b], Slawomir Bystrzanowski [a], Andreas Stark [a], Thomas Buslaps [c], Frank-Peter Schimansky [d], Rainer Gerling [d], Christina Scheu [b], Andreas Schreyer [d]

[a] *Department of Materials Science and Technology, Technical University of Hamburg-Harburg, Eissendorferstrasse 40, D-21073 Hamburg, Germany*
[b] *Department of Physical Metallurgy and Materials Testing, Montanuniversität, Franz-Josef-Strasse 18, A-8700 Leoben, Austria*
[c] *European Synchrotron Radiation Facility, BP 220, F-38043 Grenoble Cedex, France*
[d] *Institute for Materials Research, GKSS-Research Centre, Max-Planck-Strasse 1, D-21502 Geesthacht, Germany*
[e] *Bragg Institute, Australian Nuclear Science and Technology Organisation, Private Mail Bag 1, Menai NSW 2234, Australia*

Abstract

High-energy synchrotron X-ray diffraction is a novel and powerful tool for bulk studies of materials and is applied to the investigation of a high Nb-bearing γ-TiAl-based alloy. The results determined from ex situ diffraction patterns of differently heat-treated samples are compared with those from metallographic examinations. The diffraction angles and also the morphology of reflections on the Debye–Scherrer rings are evaluated in order to determine lattice parameters and grain sizes as well as crystallographic correlation. An in situ heating cycle from room temperature to 1362 °C has been conducted starting from massively transformed γ-TiAl. With increasing temperature, the occurrence of strain relaxation, chemical and phase separation, domain orientations, phase transitions, recrystallization processes, and subsequent grain growth can be observed. Finally, a fully lamellar structure, well oriented with respect to the high-temperature phase, is formed. The data obtained by high-energy synchrotron X-ray diffraction, which contain extremely rich information, are interpreted step by step and relate well with the ex situ observations and metallographic examinations.
© 2006 Acta Materialia Inc. Published by Elsevier Ltd. All rights reserved.

Keywords: Titanium aluminides; Synchrotron radiation

1. Introduction

Low density, high specific yield strength, good oxidation resistance, and good creep properties at elevated temperatures make intermetallic γ-TiAl-based alloys good candidates as structural materials for advanced jet and automotive engines as well as for future hypersonic vehicles [1–3]. The mechanical properties depend strongly on composition, thermo-mechanical processing, and subsequent heat treatments [4–6]. γ-TiAl-based alloys mainly consist of ordered tetragonal γ-TiAl ($L1_0$ structure) and ordered hexagonal $α_2$-Ti_3Al phases (DO_{19} structure) [7,8]. Standard microstructures which can be adjusted by means of heat treatments are referred to as near gamma, duplex, and fully lamellar [3,4]. In fully lamellar materials the colonies consist of sequences of several γ-phase lamellae with {1 1 1} interfaces interrupted by single $α_2$-phase lamellae with {0 0 2} interfaces [9,10]. Additionally, three different domain orientations are observed in the γ lamellae with an orientation rotation of 120° around [1 1 1]. Typically, the colony size, depending on alloy composition and heat treatment, is about 50–1000 μm with average thicknesses of 100–1000 nm of the γ lamellae and some 50 nm for the

α_2 lamellae [4–6]. Several atomic per cent of Nb sitting sub-stitutionally on Ti sites, so-called TNB alloys, may alter the recrystallization processes and thus the microstructure and mechanical properties [11,12]. The so-called massively transformed γ-phase stems from a quenching process from the α-phase field, where the constitutive elements are homogeneously distributed. The cooling rate has to be slow enough to allow a nucleation and growth process for this phase, but fast enough to prevent equilibrium phase sepa-ration. The microstructure appears irregular and disor-dered which is reflected in the diffraction pattern. The formation and the microstructural characteristics of mas-sively transformed γ-TiAl-based alloys have been investi-gated by many research groups. For further information the reader is referred to Refs. [13–16] and the references cited therein. In contrast, quenching from the $\alpha + \gamma$ field below the α-transus temperature results in a globular microstructure exhibiting well-separated α_2 and γ grains. In this paper, the different heat treatments and microstruc-tures are presented in detail and compared with their dif-fraction patterns.

The processes occurring during heat treatments are complex and difficult to study directly. Therefore, charac-terization and measurements are necessary with different techniques such as macroscopic stress and strain measure-ments, hardness testing, optical and electron microscopy, calorimetry, as well as diffraction methods with neutrons and X-rays, to mention but a few. Regarding X-rays, clas-sic laboratory devices play an important role in ex situ measurements of phases, textures, and lattice spacings (strain). In the early 1990s an in situ high-temperature X-ray diffraction study of binary TiAl alloys using Cu Kα radiation was reported which focused on the α_2 to α transition [17]. With the limited penetration of this radia-tion only near-surface sample volumes can be studied which nowadays are known to be affected by near-surface processes, such as oxidation and evaporation of Al influ-encing the composition of this region. However, novel techniques have been and are being developed with the evolution of synchrotron instrumentation. Applications investigating in situ near-surface layers of Ti–Al alloys have been investigated with 10 keV synchrotron X-rays [18]. In contrast, high-energy X-rays in the range of 100 keV and above can penetrate centimeters into light and medium-dense materials as investigated here. The high flux and intensity of modern sources give rise to high spatial and angular resolutions at high acquisition rates [19]. The combination of the penetration power into a bulk sample and the large number of photons available allow for sophisticated in situ investigations, as was per-formed in this study on a massively transformed γ-TiAl-based alloy.

2. Experimental

2.1. Materials and heat treatments

TiAl sheets of the composition Ti–46Al–9Nb (in at.%) were manufactured by using powder metallurgy approach [20]. After rolling, the material was primary annealed (PA) for 3 h at 1000 °C in order to minimize residual stres-ses. As a result of rolling processes and heat treatment, the sheet shows a fine-grained near-gamma microstructure which consists of areas with globular γ-TiAl grains with an average size of about 15 μm, which are surrounded by recrystallized regions of similar size consisting of small γ-TiAl and α_2-Ti$_3$Al grains of approximately 0.5×3 μm^2 size as shown in Fig. 1.
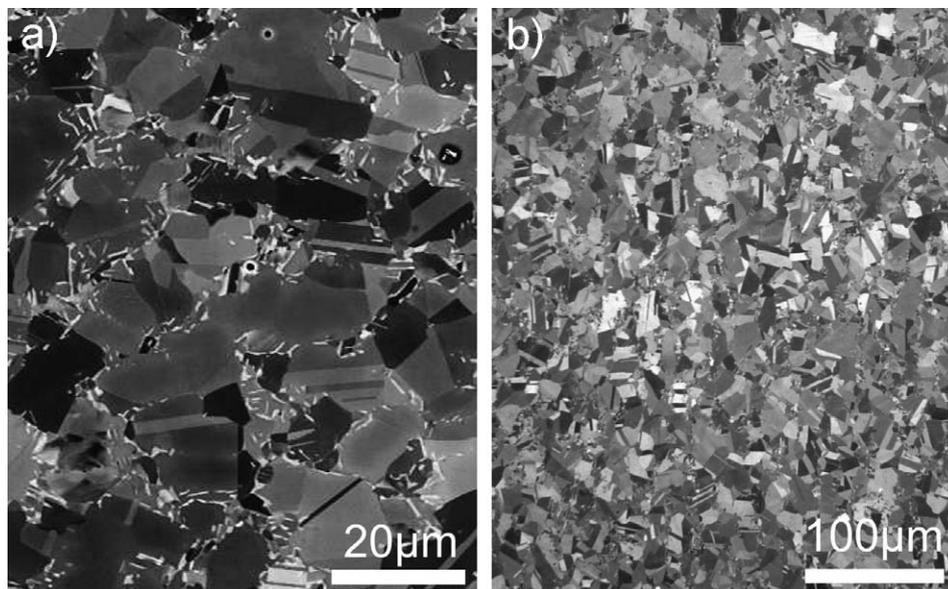

Fig. 1. Microstructure of a Ti–46Al–9Nb sheet after primary annealing (PA) for 3 h at 1000 °C. (a) SEM image in back-scattered electron (BSE) mode. Dark phase: γ-TiAl; light phase: α_2-Ti$_3$Al. (b) Optical micrograph taken with polarized light.

Samples of this starting material were used for heating for 4 min below and at the α-transus temperature $T_\alpha^- = 1280$ and $T_\alpha = 1330\ ^\circ C$, respectively, followed by quenching. During the heat treatment at T_α^- the fine-grained $\alpha_2 + \gamma$ regions in the PA material transform to globular α grains and additionally fine platelets of α grow parallel to the $\{1\,1\,1\}$ planes in γ. Transmission electron microscopy (TEM) investigations provide evidence that after quenching from T_α^- all α is transformed to α_2 but the high-temperature microstructure is preserved. This leads to an α_2-rich (AR) sample as displayed in Fig. 2, consisting of globular α_2 and γ grains with a size of about 15 μm and fine α_2 platelets in the γ grains. In contrast, oil quenches from above T_α lead to massively transformed γ-TiAl material (MT) with a microstructure as shown in Fig. 3. The irregular appearance is one characteristic of this type of microstructure. Although homogenous regions of 10–20 μm in size can be identified, they disintegrate into much smaller structures and features. Thus, a typical grain size cannot be found but there is a
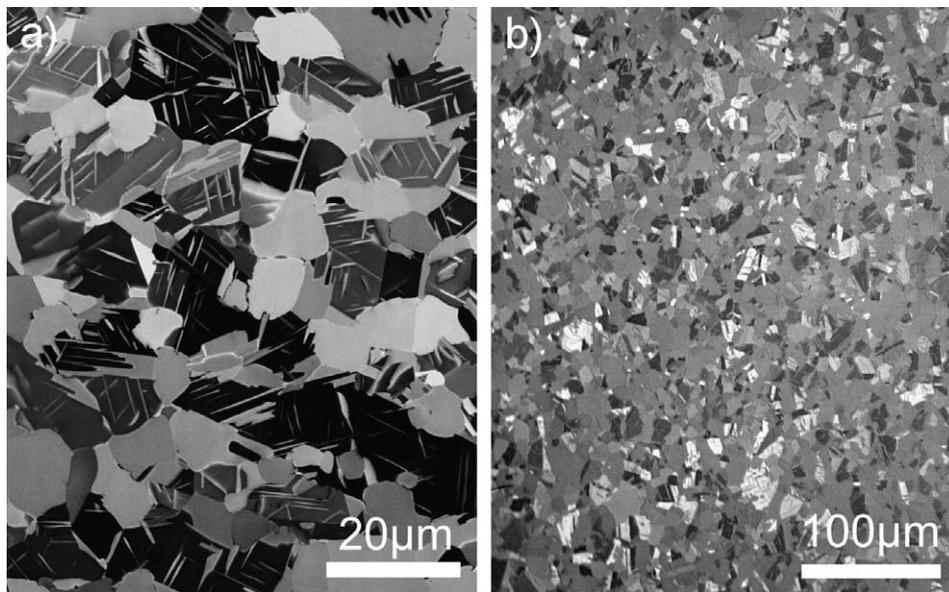

Fig. 2. α_2-rich (AR) microstructure of a Ti–46Al–9Nb sheet sample after annealing for 4 min at 1280 $^\circ$C and subsequent oil quenching. (a) SEM image taken in BSE mode. The α_2-grains appear as light gray phase and the γ-grains as dark gray phase showing crossed light α_2 laths. (b) Optical image taken with polarized light.
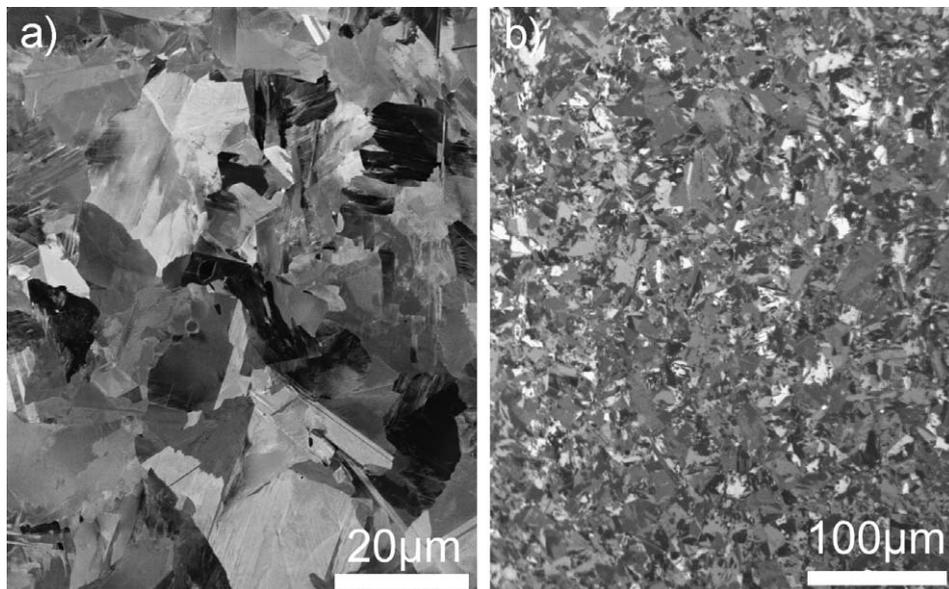

Fig. 3. Microstructure of a massively transformed (MT) Ti–46Al–9Nb sheet after 4 min of heat treatment at 1330 $^\circ$C and subsequent oil quenching. (a) SEM image in BSE mode; (b) optical micrograph.
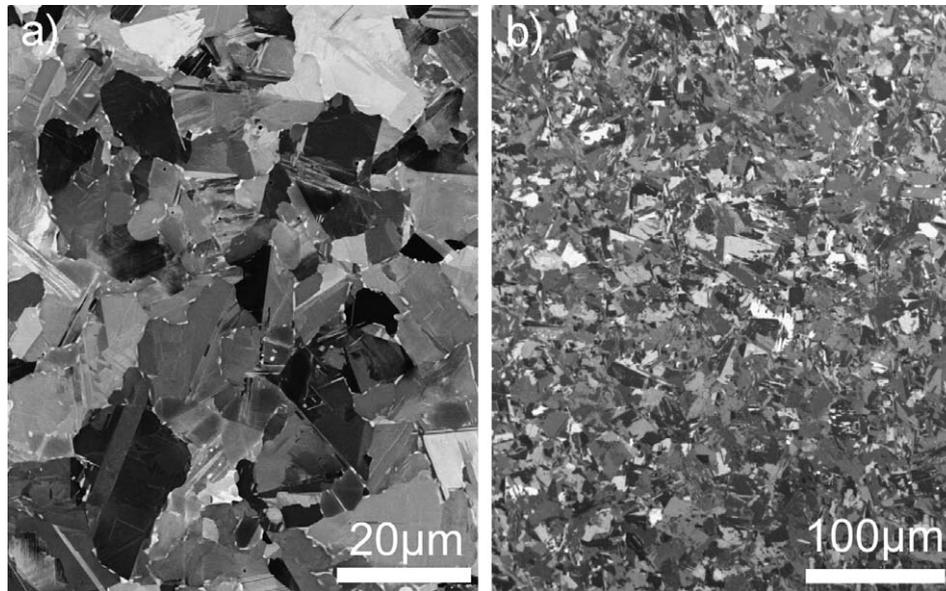
Fig. 4. Microstructure of massively transformed Ti–46Al–9Nb sheet after annealing for 1 h at 1000 °C (MTA). (a) SEM image in BSE mode exhibits small α_2-precipitates (light contrast) at γ-TiAl grain boundaries. (b) Micrograph obtained under polarized light.

distribution from 1 to 20 μm. Smooth grain boundaries are extremely rare which is a general feature of massively transformed materials [13–15,21]. One of the MT samples was further annealed (MTA) for 1 h at 1000 °C and then slowly cooled. The resulting microstructure is shown in Fig. 4. Obviously, a recrystallization process has taken place. The rough and irregular microstructure has developed into a more homogeneous one. Smooth grains of a similar size distribution have been formed; however, they are still distinct from the globular structure of the PA material and small α_2-precipitates can be observed at the γ-TiAl grain boundaries.

Another MT sample (IMT) was used for running a heating cycle in situ under X-ray diffraction below and above the α-transus temperature. IRE denotes the IMT sample heated above T_α and subsequently re-entered the $\alpha +$ γ-phase field. Fig. 5(a) and (b) represent the microstructure before and after the heating cycle, respectively. The IMT sample is similar to the MT sample, but shows a larger grain size distribution up to 40 μm. The IRE sample that was held above T_α exhibits a fully lamellar microstructure with a colony size of about 500 μm. The colonies consist of coherent stacks of thin α_2- and γ-lamella. The (0 0 1) basal plane of the hexagonal α_2-Ti$_3$Al fits best to the (1 1 1) planes
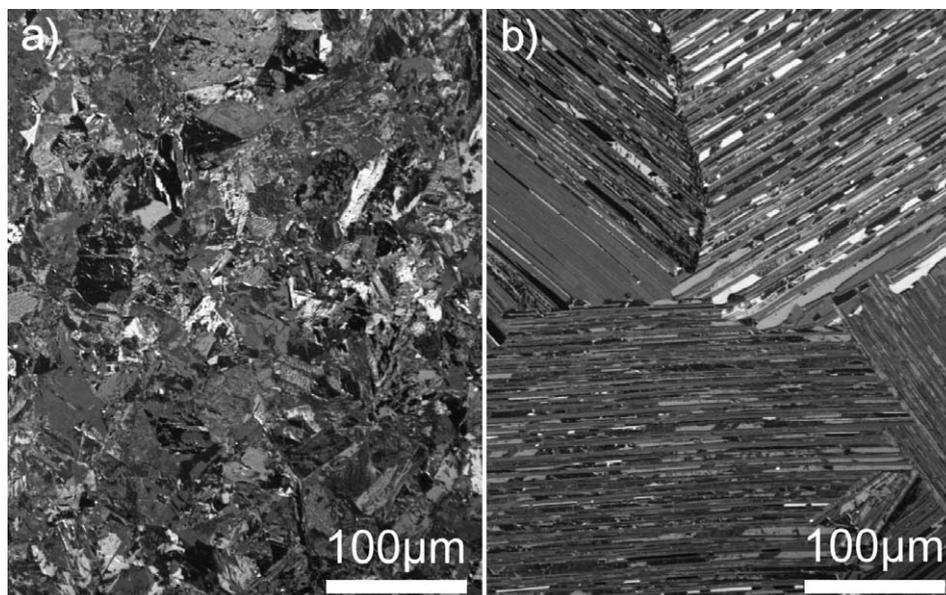

Fig. 5. (a) Initial microstructure of a massively transformed (IMT) Ti–46Al–9Nb sample which runs in a heating cycle with in situ observation of the X-ray diffraction pattern. (b) Lamellar microstructure at the end of the heating cycle (IRE). Both images obtained with polarized light.

Table 1
Summary of samples used in the present investigation

Sample	Association	Description
PA	Primary annealed	Starting material, globular sheet, γ-rich
AR	Rich in α_2	PA tempered for 4 min at 1280 °C, oil quenched
MT	Massively transformed	PA tempered for 4 min at 1330 °C, oil quenched
MTA	Massively transformed and annealed	MT annealed 1 h at 1000 °C
IMT	In situ massively transformed	MT used for in situ heating cycle
IRE	In situ re-entrant	IMT heated above the α-transus temperature and subsequently re-entered the γ + α-field

of the slightly tetragonal γ-TiAl lattice which form an interface with high coherency. Due to the threefold rotation symmetry of the (1 1 1) plane of the almost cubic γ-structure, there are three possible orientations to align two adjacent γ-lattices, leading to three individual domains. Further, a spontaneous change of the stacking sequence of the atomic γ-(1 1 1) layers leads, together with the three domain orientations, to three further twin orientations. These possible variants give rise to orientation contrasts within one single lamella.

A compilation of the different samples is given in Table 1.

2.2. Diffraction setups

High-energy X-ray diffraction setups were used at both the PETRA-II beamline at HASYLAB/DESY in Hamburg and the high-energy beamline ID15B at the ESRF in Grenoble. The benefits of X-rays in the range around 100 keV, as employed in the present study, are the high penetration power which allows the study of bulk properties of samples, the small diffraction angles of a few degrees, permitting one to obtain diffraction patterns in the forward direction through the small optical apertures of a diffraction furnace, the large radius of the Ewald sphere allowing smooth take off from the lattice plane in reciprocal space and probing the diffuse scattering around the sharp Bragg positions. A review of the techniques and applications is given in Ref. [19]. We used the transmission setup with a two-dimensional image-plate detector.[1] An incident beam of approximately 90 keV and lateral dimensions of 100–1000 μm strikes the polycrystalline sample. According to Bragg's law and the considered lattice spacing, individual crystallites scatter to different Debye–Scherrer rings, which are registered on the image plate. The radius of the rings is directly related to the scattering angle 2θ and thus to the d-spacing, whereas the intensity distribution along one ring is related to the orientation distributions of grains. Thus, the distribution delivers the texture of the material [22], while the morphology of sharper spots in the rings can give information about the orientations of individual grains [23].

At PETRA-II, diffraction patterns of the different PA, AR, MT, and MTA samples were recorded at room temperature. The distance between the sample and the detector

is a major factor in the evaluation of the lattice parameter and therefore a theodolite was adjusted perpendicular to the incident beam in order to position the sample reproducibly to an accuracy better than 100 μm. Refinement from a body-centered cubic (bcc)-Fe diffraction pattern leads to a mean detector distance of 972 mm and an X-ray energy of 89.0 keV. However, careful fitting processes reveal that the detector plane was off horizontal by 1.5° to the normal of the incident beam, which makes accurate data processing more difficult to perform. Since we looked only to relative changes of individual lattice spacings, the error cancels and thus this problem was not pursued further. The beam size was not smaller than 500×500 μm^2.

In situ observations during a high-temperature heating cycle were undertaken at ID15B with a narrow beam of 100×100 μm^2. A piece of the massively transformed sample IMT with a cross section of about 1 mm^2 was mounted on a ceramic holder of an ESRF-designed diffraction furnace. The latter device operates in air, and consists of a vertical boron nitride tube of 10 mm diameter and 100 mm height. The mantle contains a KANTHAL heating element, reaching temperatures up to 1400 °C. The temperature measurement had a significant systematic error, in particular when running a ramp, and was recalibrated to the α-transus temperature $T_\alpha = 1330$ °C, as obtained from other measurements. This gives consistence with the ex situ data. Entrance and exit holes in the furnace, 1 mm and 7 mm in diameter, were used for the incident beam and the diffracted Debye–Scherrer cones, respectively. A heating cycle as represented in Fig. 6 was run and diffraction patterns were recorded every 275 s. This acquisition time results from 45 s for exposure plus detector read-out, erasing, and monochromator tuning. Again, a bcc-Fe pattern was measured for calibration prior to the experiment revealing a sample to detector distance of 1282 mm and an X-ray energy of 94.4 keV. In particular, the detector was perfectly aligned towards the beam axis. It was held on a well-aligned diffractometer table and could be translated reproducibly into and out of the beam. The sample position could be scanned comfortably using an alternative PIN diode measuring the shadow in the direct attenuated beam behind the sample.

For all data, the non-dispersive point [19] is to the left of the ring center, the rolling direction of the sheet vertical and the transverse direction horizontal, unless stated differently. Reflections of the γ-phase are indexed according to the tetragonal lattice, while both hexagonal phases α and

---

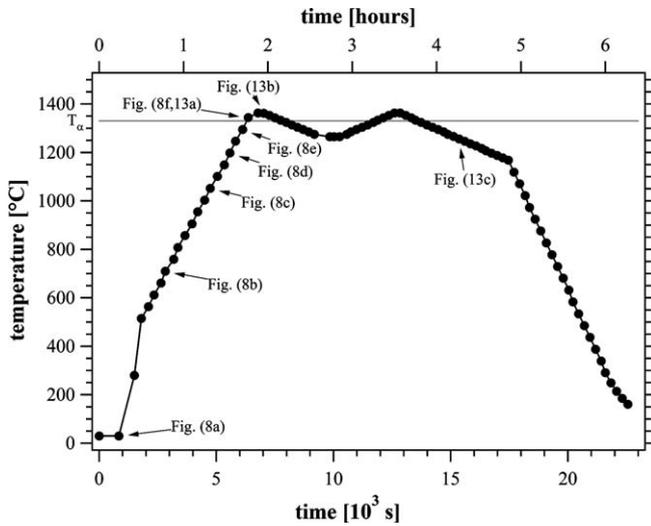[1] Model mar345 by marresearch GmbH, Norderstedt, Germany; http://www.marresearch.com/.

Fig. 6. Heating cycle used for the in situ experiment. Indicated are where Figs. 8 and 13 were taken. T_α is the α-transus temperature of Ti–46Al–9Nb (~1330 °C).

α_2 are indexed according to the larger unit cell of the ordered phase α_2 containing two formula units of Ti$_3$Al.

3. Results and discussion

3.1. Diffraction data obtained at room temperature

Experimental Debye–Scherrer patterns as obtained at PETRA-II are compiled in Fig. 7. The Miller indices of important reflections are indicated. According to the Ti–Al phase diagram, all of the patterns show more or less the coexistence of both phases, i.e. γ-TiAl and α_2-Ti$_3$Al. The α-phase usually orders below the eutectoid temperature to α_2-Ti$_3$Al. The larger unit cell of the ordered phase will be used throughout the article to describe both hexagonal phases, leading to the extinction of certain reflections when disordered. Generally, the morphology of the Debye–Scherrer rings is related to grain size and grain shape with respect to beam size and dimensions of the illuminated
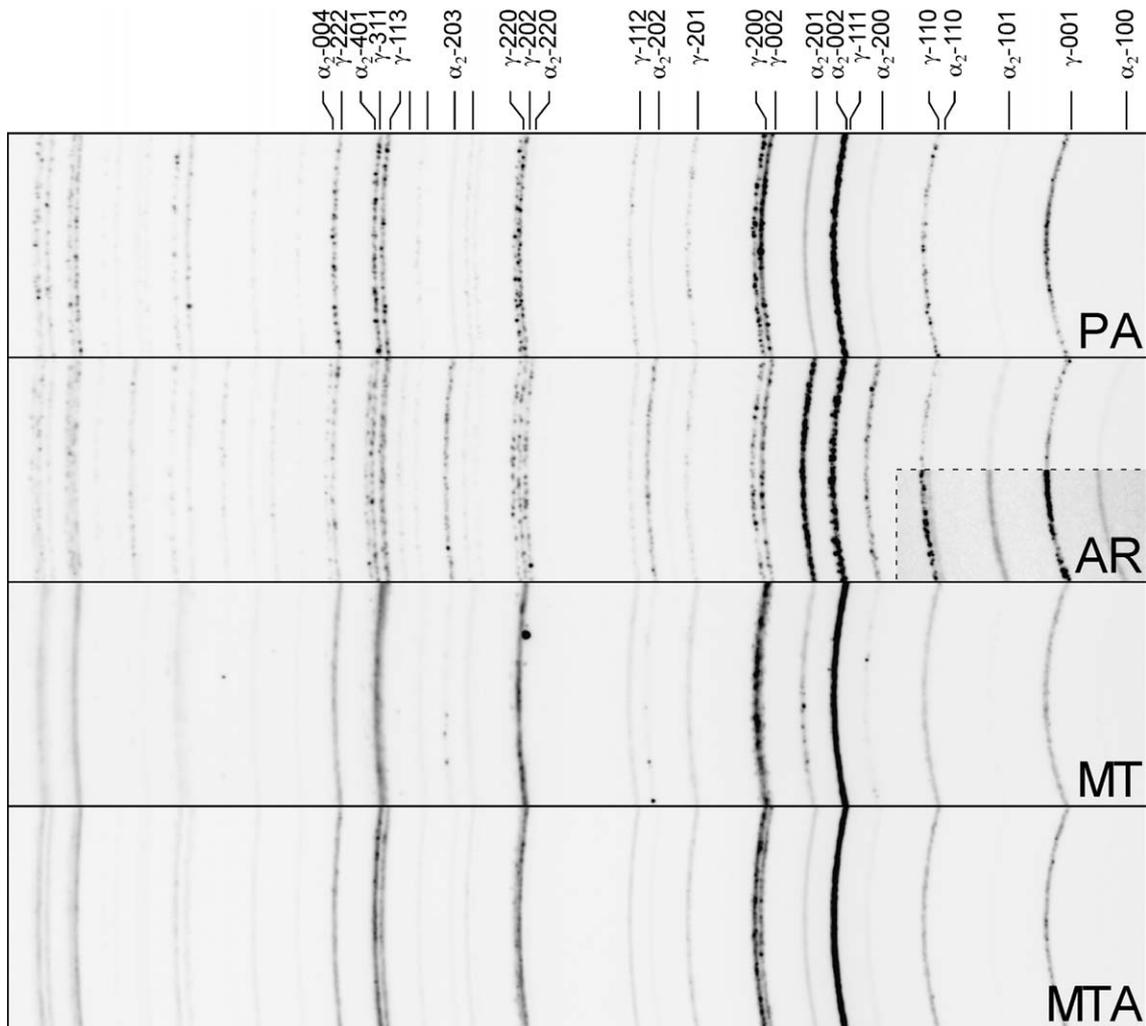

Fig. 7. Extracts of the raw data in the reciprocal space direction around the non-dispersive point [19], i.e. the direction of best resolution obtained at PETRA-II for the room-temperature measurements. The Debye–Scherrer rings are indexed at the top. Characteristic differences of the diffraction patterns can be seen for the individually heat-treated specimens (see Table 1). The inset for the AR material is displayed with a different gray-scale in order to enhance the weaker α_2-Ti$_3$Al rings.

volume. A spiky pattern reveals the reflections of relatively few large grains, while a continuous and smooth ring indicates a much higher number and therefore much smaller grains.

This is nicely demonstrated for the PA material (Fig. 7), where the γ-rings exhibit a spiky pattern and, simultaneously, almost no features can be distinguished in the α_2-rings. This is consistent with the micrographs shown in Fig. 1, where larger γ-grains and also a minor volume fraction of small recrystallized γ-grains and much smaller α_2-grains are observed. Closer inspection of the γ-rings reveals the continuous contribution of the small grains superimposed by the spiky pattern of large grains, respectively.

The tetragonal structure of the γ-TiAl phase deviates only slightly from the cubic face-centered cubic (fcc) structure [4]. Therefore, rings with interchanged Miller indices $hkl \rightarrow lkh$ appear in double features, such as 002/200, 202/220, 113/311, etc. Their splittings, i.e. their differences in the scattering angles, are directly related to the c/a ratio of the tetragonal γ-TiAl unit cell.

The diffraction pattern of the AR material shows stronger α_2-rings in accordance with the microstructure shown in Fig. 2. About 50% of the volume, not only the platelets but also globular grains which appear light gray in Fig. 2, consists of α_2-phase. These globular α_2-grains are verified by TEM investigations, which are the subject of a forthcoming publication. The high α_2 content is confirmed by the high intensity of the α_2 peaks in Fig. 11. The larger number of α_2-rings is due to the lower symmetry as compared with the γ-phase. In a first view, the α_2-002 ring coincides with the γ-111, demonstrating that the change in structure from the almost fcc to the almost hexagonal close-packed lattice is just a change in the stacking sequence along ⟨111⟩. Careful observation reveals that the α_2-002 spots are slightly shifted to larger scattering angles than γ-111. The crystallographic relation of the almost coherent fitting between the α_2-(001) and the γ-{111} planes appears as well in the ring triplet α_2-220, γ-202, γ-220, which almost show identical diffraction angles. This correlation is well known as the Blackburn relationship [24]. The Debye–Scherrer rings of AR are very spiky indicating large grains for both the α_2- and γ-phase, which again is in accordance with the prevailing microstructure (Fig. 2).

The patterns of the MT material differ strongly from those of the PA and AR samples. Although quenched at a similar rate, AR originates from the $\alpha + \gamma$-phase field close to T_α, while MT starts from a pure α-phase. In the former, α transforms to α_2 but the high-temperature structure is preserved, while the latter transforms almost exclusively into the massive γ-phase [15]. In contrast to the PA rings the diffraction patterns are blurred both radially, relating to longitudinal lattice strain, and azimuthally, showing huge mosaic spreads of individual grains or correlated groups of grains. In particular, the above mentioned double features with interchanged Miller indices wash out

to radially broad distributions as demonstrated at the γ-002/200, 202/220, 113/311 rings. There are hints that both rings of the pairs are distinguishable with a small splitting, well apparent on γ-002/200, but there is a large contribution of reflections lying between the small splitting of scattering angles. The radial distribution gives evidence that small grains nucleate into different domains with the a-axis roughly parallel to the c-axes of a neighboring domain, stressing the a- and c-direction in tension and compression, respectively, and thus broadening the reflection. Similar orientation relationships of γ domains in massively transformed γ grains have been found in TEM images [21]. Together with the appearance of the superstructure reflection γ-001, we have to conclude that the γ-phase is ordered. The degree of ordering, however, cannot be specified. The huge mosaicity of several degrees can be deduced from the rings γ-202/220 in Fig. 7 which shows three broad accumulations of intensity along the ring. Each of these regions may originate from a single, very large α-grain which transforms upon quenching into a variety of small massive γ-grains which are rotated towards each other by more or less small-angle boundaries as evidenced by means of electron back-scattered diffraction [15,21]. Again in agreement with the microstructure in Fig. 3, there is no typical spot size/grain size, but a large distribution from smooth ring components/small crystallites to individual bright spots/large grain sizes.

The appearance of the pattern sharpens again after annealing as shown in Fig. 7 for the MTA sample. The material is recrystallized and internal stresses relaxed, which is reflected in the splitting of the double-featured rings, although it is smaller than that for the PA or even the AR material. A smooth intensity distribution on the α_2-rings relates to fine particles of the α_2-phase [15,16]. Spot size distribution and smoothness again correspond well with the microstructure shown in Fig. 4.

3.2. In situ heating of MT specimens

Larger ring sections as obtained from the IMT experiment are compiled in Fig. 8 for different temperatures upon heating. The pattern shows the same features at 25 °C as for the MT sample (Fig. 7), i.e. the splitting of the γ-200/002 reflections is smeared as described (Fig. 8(a)). Due to the smaller beam size by a factor of 5 in each dimension, reflections from fewer grains are present. In particular, single grains or groups of grains can be observed throughout the heating cycle. Thermal recovery or recrystallization is still negligible at 710 °C and the overall distribution of intensity along the rings remains unchanged (Fig. 8(b)). The splitting of the double feature of γ-200/002 rings, however, begins to become more distinct which can be accounted for by the relaxation of the huge stresses bringing the a- and c-axes to each other. At 1052 °C (Fig. 8(c)), the splitting enlarges and the mosaicity of the grains strongly reduces in order to form string-of-pearls-like patterns of intensity at 1198 °C (Fig. 8(d)). In
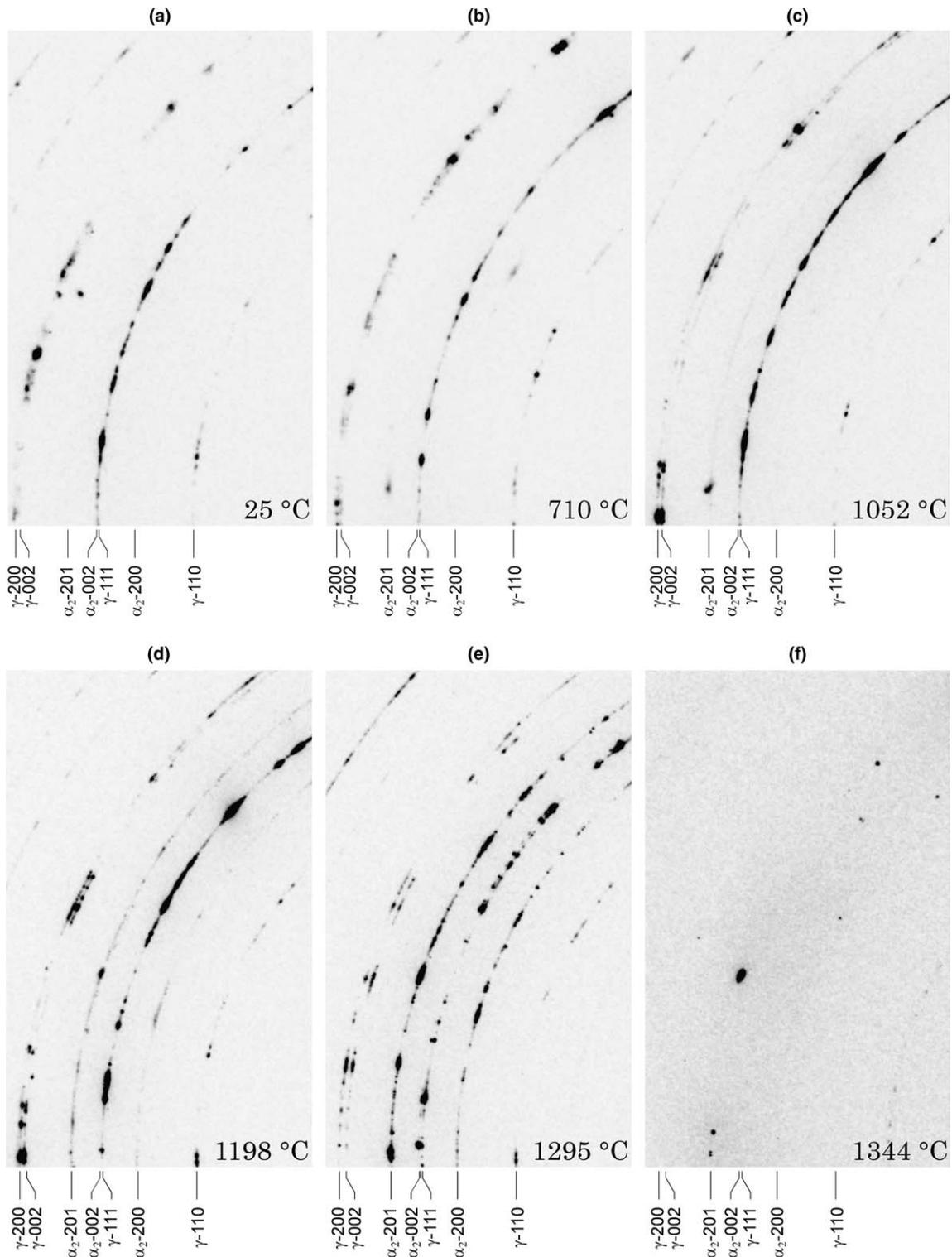
Fig. 8. Sections around the non-dispersive point [19] of the full Debye–Scherrer rings at selected temperatures of the in situ experiment at ID15B. The origin of the reciprocal space, i.e. the common ring center, is to the right at the bottom. Features such as the splitting of the γ-002/200 rings, the morphology, and the ratio of α/γ phases evolve within the heating cycle (see Fig. 6).

addition, the contribution of the growing α_2-phase, and later on the α-phase, becomes stronger. Just below the α-transus temperature, at 1295 °C, in Fig. 8(e) we observe in situ the α-rich pattern similar to that of the AR sample. The splitting has grown to a maximal value and the string-

of-pearls-like patterns are further developed. Finally, at 1344 °C, the system has undergone the $\alpha + \gamma \rightarrow \alpha$ transition and the material has completely transformed to large α-grains, leading to a very few spots on the detector (Fig. 8(f)).

The data obtained in this heating cycle can be evaluated with regard to azimuthal and radial distributions of intensities. This allows us to describe in more detail mosaic and angular correlations or grain statistics as well as thermal expansion or the splitting of the double feature.

3.3. Ring morphology: influence of the γ-TiAl domain structure

The morphology of the rings gives evidence for the correlation between grains. Intensity distributions often find their counterpart on rings which are split due to their tetragonal deviation from the cubic lattice, such as the data for γ-200 and γ-002 represented in Fig. 9 which were extracted from the pattern taken at 1295 °C (Fig. 8(e)). A reflection observed on one of the rings finds its partner on the other, often face-to-face and sometimes shifted by a small azimuthal angle. We can attribute this observation to the coherent fitting of different γ-TiAl domains as introduced above: Upon ordering, there are three different ways to orientate spontaneously the c-axis in space along the three orthogonal base orientations of the γ-TiAl unit cell. For a cubic system, this means there are three different possibilities to orient the pyramid as cut from the unit cell by the (111) plane onto the latter leaving the structure unchanged. This threefold symmetry is broken when the cubic system becomes tetragonal distorted and the orientation of the c-axis describes the three domains. Coherent fitting of the atoms at a common (111) domain wall relates to an angular shift of two adjacent domains, as sketched in Fig. 9. This demonstrates the situation in the common $(\bar{1}10)/(01\bar{1})$ plane of drawing separated by a coherent (111) interface. The c- and a-axes to the left are interchanged with a- and c-axes to the right, respectively, and have to fit together on (111), resulting in the angular shift Δv between the swapped lattice and the continued lattice, here shown dashed, of the neighbor domain. The side lengths of the triangles shown and simple trigonometric consideration gives the angular shift
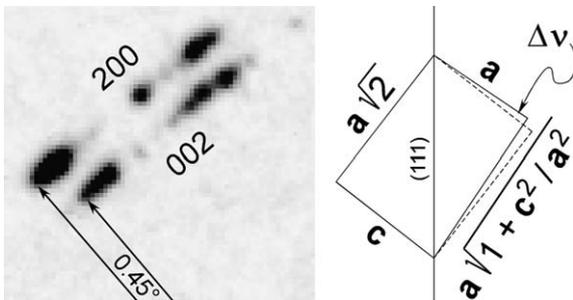
$$\Delta v = \arctan\left(\frac{c}{\sqrt{2}a}\right) - \arctan\left(\frac{1}{\sqrt{1 + c^2/a^2}}\right) \qquad (1)$$

The c/a ratio can be obtained from the splitting of the rings and is 1.011 for this case, resulting in $\Delta v = 0.45°$ as shown in Fig. 9. This coincides perfectly with the observed azimuthal shift between the spots observed on the 200 and 002 rings and nicely validates this model of coherent domain growth. Thus, the c/a ratio represents an important quantity for both the radial splitting and the azimuthal shift at domain boundaries. As mentioned, not all of the correlated reflections show this azimuthal shift: some are face-to-face opposite to each other, which is due to the three-dimensional orientation of the crystallites to the scattering vector. This maximal shift Δv is solely observed if the common $(\bar{1}10)/(01\bar{1})$ plane is perpendicular to the incident beam minus the Bragg angle. Otherwise, only the projection is seen which can reach a zero component in the plane of observation.

The observation of such a domain structure underlines the situation of the stress model of the initial IMT material at 25 °C, where the double feature of the γ-200/002 rings is barely seen in favor of reflections lying between, notably from spontaneously created microdomains distorting strongly the lattice of their neighbors. Further, the domain relationship can explain the string-of-pearls-like patterns, which then are just a series of adjacent domains stacking up. Depending again on the three-dimensional orientation of each, the azimuthal shifts can add up to larger values. It is tempting to speculate that recrystallization starts from a more or less random micrograin pattern with a high energy of distortion leading to individual large domains which then rearrange in order to form low-energy domain walls. Larger orientational misfits can be bridged by means of an appropriate stacking of domains. At higher temperatures and longer annealing times the domains coarsen in order to further minimize the energy.

We note that similar pairs of reflections are found on the γ-111/α-002 rings which gives evidence for the well-known coherent growth of the two phases at the common interface as described for the AR and the IRE samples. Thus, the atomic arrangement in the γ-(111) and α-(002) planes represents a fundamental issue which occurs during phase transitions, recrystallization, domain formation, and twinning. Other common directions in which the atomic patterns have to fit coherently are the directions perpendicular to this plane, i.e. represented by the reciprocal lattice vectors of the α-220 together with the γ-202 and the γ-220 types. An extract of the diffraction pattern at 1295 °C is given in Fig. 10, showing these correlations between domains and grains of the different phases. Misfit, however, results in longitudinal stress as revealed in the next section.

3.4. Ring diameter: evaluation of lattice parameter

Classic powder diffraction patterns are obtained after integration of the rings around one turn or over a larger

Fig. 9. Detailed extract of a γ-200/002 ring pair (left), obtained from the IMT sample at 1295 °C, with two radii vectors pointing from the center into the figure, showing correlations between reflections on both rings. They can be interpreted as reflections from adjacent domains coherently linked by a (111) domain wall, as demonstrated in the schematic on the right-hand side.
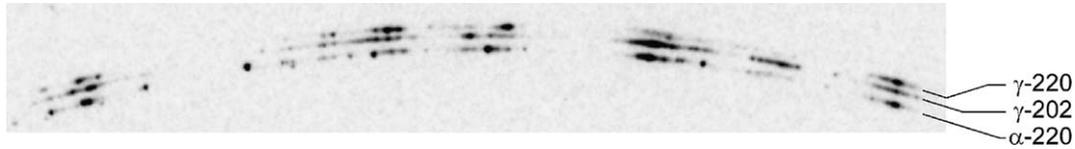
Fig. 10. Ring triplet obtained from the IMT sample at 1295 °C showing correlations between the γ- and α-phases, which are coherently correlated by the Blackburn relationship, and domain orientations. Features from one of the rings appear on the others, either face-to-face or shifted by a small-angle grain (domain) boundary, depending on the projection.

sector of 30° as done for the present evaluation. Extracts of the region between the α/α₂-200 and γ-200 of the patterns are compiled in Fig. 11 for all four ex situ measurements, Table 1, and different stages of the in situ experiment in Fig. 6. This was used to evaluate the positions of the γ-reflections 111, 002, and 200. Lorentzians have been fitted for all of them and the width of the $002/200$ peaks has been kept constant to the value of the single reflection when they superimposed. This procedure always leads to a numerical splitting, even in the case of a single, broad peak. The real shape of the peaks is difficult to simulate systematically and has to be discussed in terms of the two-dimensional data. Fig. 12(b) shows the peak positions as they develop for different material conditions or test tempera-

tures. It shows the relative values normalized to the room temperature values of the MT and IMT samples. Further, the temperature evolution of these reflections is given for the IMT and one representative data point for the IRT sample. The nomenclature

$$\Delta G/G \left(h\,k\,l \div h'\,k'\,l'\right) \approx -\Delta d/d \left(h\,k\,l \div h'\,k'\,l'\right) := \frac{R_{h\,k\,l} - R_{h'\,k'\,l'}^{\mathrm{MT}}}{R_{h'\,k'\,l'}^{\mathrm{MT}}}$$

(2)

denotes the relative change of the scattering vector $\Delta G/G_{h\,k\,l}$ with respect to $G_{h'\,k'\,l'}^{\mathrm{MT}}$ which is, for small variations and simplified by the linearized form $G \sim R$ of Bragg's law and the scattering geometry as valid for small Bragg angles, equal to the relative change of the ring radius R and the negative value of the change in the relative lattice spacing $\Delta d/d$.

Considering the behavior of the 111 reflection, one can extract the thermal expansion, which has been fitted in second order and results in

$$\Delta G/G \left(T\right) = -8.8909 \times 10^{-6} T - 2.6057 \times 10^{-9} T^2 \quad (T \text{ in } °C)$$

(3)

as represented by the underlying gray line. A linear thermal expansion coefficient of $1.4 \times 10^{-5}\,\mathrm{K}^{-1}$ at 1000 °C can be extracted for the γ-TiAl phase embedded in the microstructure. The 200 reflection shows exactly the same expansion behavior until it deviates just below the phase transition at 1295 °C while the course of the 002 reflection behaves similar until ~930 °C and then deviates more rapidly to smaller ΔG values. The offset of the curve belonging to 002 shows the splitting of the double-featured rings. Although equidistant until 930 °C, the profile changes from a broad, single-appearing peak in Fig. 11 to a peak with a shoulder as described in the discussion of the morphology of the ring structure above. Consistently, it broadens further and then splits into two well-separated peaks which diverge at 1295 °C. According to Fig. 8, all γ-peaks disappear above the α + γ → α phase transition. Some of them reappear upon reentering the α + γ-phase, but only if the then much larger and thus much fewer crystallites are oriented close to the reflection condition. Tails of one pair of the considered reflections could be evaluated and are shown as IRE at 1227 °C in Fig. 11. The striking feature of this pair is that the splitting is much larger than previously observed. In addition, the 002 reflection is quite sharp, while the 200 seems to be composed of several parts of a broader distribution.
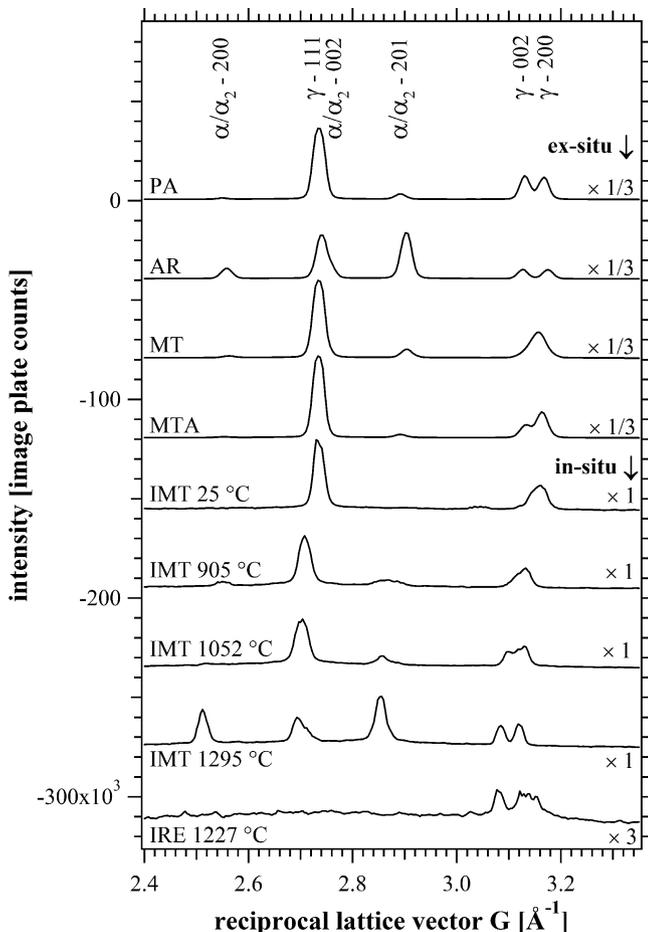

Fig. 11. Sections of powder diffraction patterns obtained after integration of the azimuthal angle of the Debye–Scherrer rings shown for ex situ and in situ measurements.
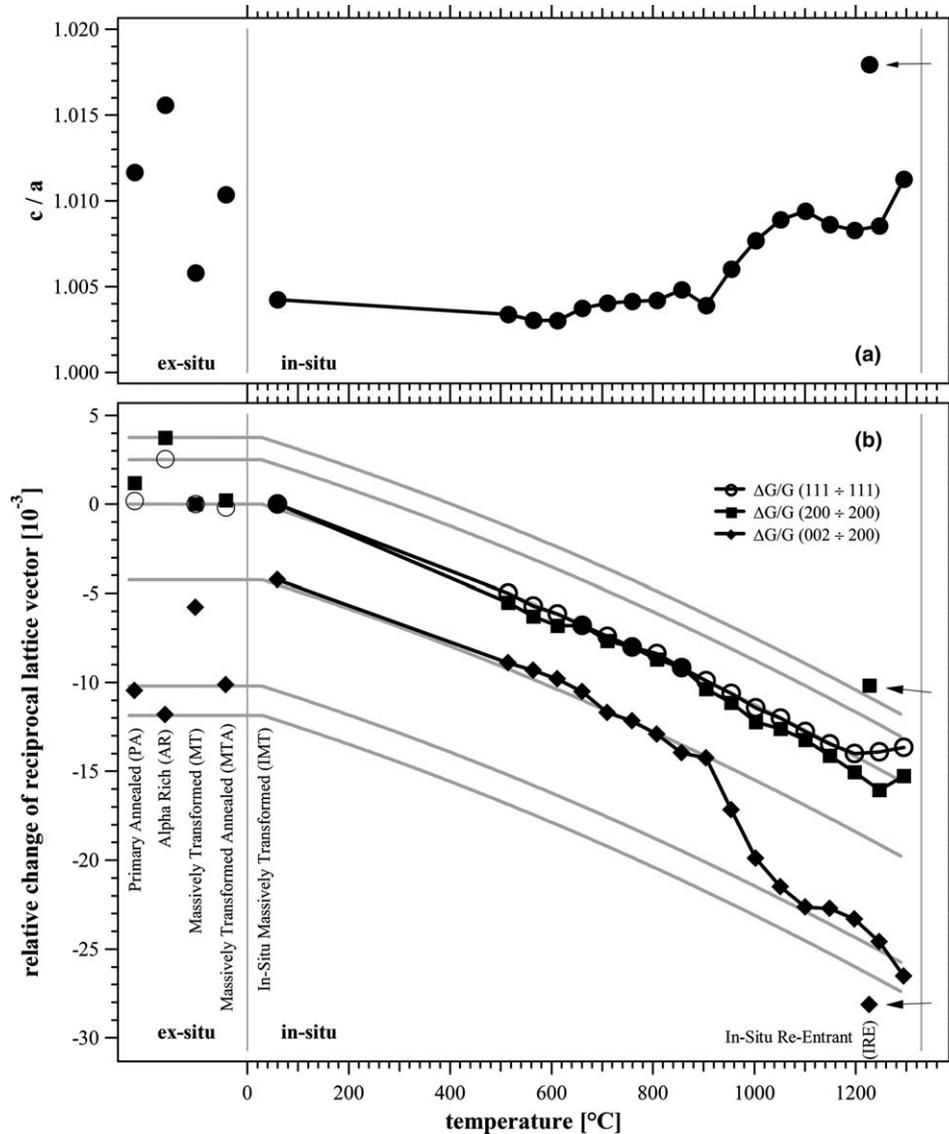
Fig. 12. Tetragonal c/a ratio and relative changes of reciprocal lattice vectors for selected reflections for the different sample variants. For the IMT condition the temperature-dependent behavior is shown. The gray lines represent the thermal expansion fitted to the γ-111 reflection, projecting the ex situ measurements with the in situ data. The three arrows to the right indicate the data points obtained after cooling from the α-phase (see Fig. 6).

The splittings of the IMT experiment can be compared with the ex situ measurements as shown in Fig. 12. Parallel, gray lines projecting the ex situ to the in situ values are shown according to the overall thermal expansion. Here, the splitting of the MT sample is minimal and falls consistently well together with the value of the IMT material at room temperature. The MTA splitting is similar to the in situ value at above 1000 °C although it is slightly increased which we attribute to the longer annealing time. The AR values correspond to the IMT values below the phase transition, and the PA values, lying somewhere between, do not have a direct counterpart. Altogether, the splittings for the ex situ samples are consistent with the in situ observations; however, being shifted due to thermal expansion.

The splitting of the γ-002/200 rings is directly related to the c/a ratio of the tetragonal γ-TiAl unit cell according to

$$c/a = 1 + \Delta G/G\,(200 \div 200) - \Delta G/G\,(002 \div 200) \quad (4)$$

as displayed in Fig. 12(a) and can be interpreted in the following way. Upon production, the MT (and IMT) material is quenched rapidly from the disordered pure α-phase, which is a homogeneous solid solution of (Ti,Nb) and Al atoms. During massive transformation long-range diffusion does not take place; therefore the formation of α2 phase is suppressed. As a consequence, the evolving γ-TiAl phase is not stoichiometric and far from chemical equilibrium. In addition the presence of high internal stresses is suspected [15]. For high Nb-containing TiAl alloys it has been shown that Nb atoms substitute Ti sites exclusively [12]. Thus, in the massively transformed Ti–46Al–9Nb alloy the γ-phase can be written as (Ti,Nb)–46Al exhibiting a surplus of Ti and a lack of Al sites. This implies that Ti-like atoms occupy 4% of Al sites within the MT material. Due to symmetry

relations a disordered γ-structure is assumed to be cubic and the described deviation from stoichiometry can be regarded as a superposition of a stoichiometric and a disordered part, thus pushing the overall lattice more into the direction of a cubic lattice, i.e. the c/a ratio approaches 1. Indeed, first ab initio calculations have shown that Ti and Nb atoms on Al sites reduce the c/a ratio of the tetragonal TiAl cell to approximately 1 [25]. Atomic diffusion starts to play a role upon heating above 930 °C. Here the α_2-Ti$_3$Al phase begins to form and Ti as well as Nb atoms from the γ-phase partition into the α_2-phase. Consequently the former gets closer to stoichiometry, thus decreasing the 'cubic' part and increasing the c/a ratio. At the eutectoid temperature of ~1170 °C for Ti–46Al–9Nb the α_2-phase disorders into α-phase which retards the separation process due to the endothermic reaction taking energy from the diffusion process. This mechanism leads to the kink in the γ-002/200 splitting curve and the local minimum in c/a shown in Fig. 12(a) and (b), respectively. An early in situ diffraction study investigated the α_2- to α-transition in different binary TiAl alloys. A comparable sluggish transition behavior was observed [17]. Upon heating to the α-transition at 1330 °C a further increase of c/a takes place due to enhanced diffusion and chemical separation. Heating above T_α transforms the sample completely into pure α-phase. Subsequent slow cooling to the $\alpha + \gamma$-phase field (Fig. 6) leads to the generation of a lamellar microstructure. The lamellar structure as displayed in Fig. 5 has been developed by chemical separation. Due to the slow cooling rate the γ-phase has sufficient time to approach its equilibrium composition and therefore the highest c/a ratio of 1.018 is obtained.

It is worth noting that the expansion of the 200 reflection is linked to the overall thermal expansion as also observed for the 111 reflection, while the 002 reflection deviates from this characteristic only above 930 °C. Spontaneously, one would expect the conservation of the volume of the unit cell upon change of the c/a ratio, which would reflect in a symmetric deviation from the mean thermal expansion with a weighting of 1/3 and 2/3 for the a- and the c-axes, respectively. The observation underlines the aspect of chemical separation of the non-stoichiometric Ti and Nb atoms: these atoms have to migrate into α-precipitates, which grow coherently to the γ-grains. Here, the atomic patterns along γ-[220] and γ-[202] have to fit onto that of α-[220]. The diffraction pattern of the AR sample (Fig. 7) and that of the IMT sample displayed in Fig. 10 reveal that they do not fit exactly and the scattering vectors behave as

$$G(\alpha\text{-}220) < G(\gamma\text{-}202) < G(\gamma\text{-}220) \qquad (5)$$

i.e. there must be a misfit in the coherence condition, to which ideally all G should be equal. Thus, the α-phase stresses the reciprocal lattice spacings to smaller values which locks in and holds the 220 value rather than increasing it. Accordingly, the 202 value decreases faster than expected, which itself reacts to the change of the c-parameter. Approaching the α-transus temperature, the α-grains

increase in size and volume fraction; thus the number of interfaces to the γ-grains is reduced leading to a decrease of misfit stress. At 1295 °C, the 200 behavior deviates towards the above mentioned constant-volume argument of the γ-unit cell and the values for the IRE sample are fully relaxed. Moreover, the 1/3–2/3 ratio of the deviation from the mean thermal expansion is fulfilled.

3.5. Transformation to α- and re-transformation to lamellar $(\alpha + \gamma)$-phases

Rapid nucleation and grain growth kinetics are observed above $T > T_\alpha$, where the system transforms to pure α-phase. A set of three typical diffraction patterns is shown in Fig. 13(a)–(c). The first pattern (after rotation, Fig. 13(a)), obtained at 1344 °C is the identical measurement from which Fig. 8(f) was extracted. Fig. 13(b) and (c) correspond to the maximum temperature of 1362 °C (see Fig. 6) and to a data set recorded after re-entering the $\alpha + \gamma$-phase field and cooling to 1256 °C, respectively.

The typical ring pattern of the initial material fades rapidly when heating above T_α. First, all the γ-phase disappears, leaving spots only on the α-rings. Extensive grain coarsening leaves only a few groups of sharp spots such as around the α-002, 201, 20$\bar{1}$, and 00$\bar{2}$ positions in Fig. 13(a). Although on different adjacent rings, these groups rearrange further when obtaining another pattern only 275 s later. However, this pattern does not differ from the next one presented in Fig. 13(b), showing a regular pattern of diffuse spots. These stem from one large, single grain. The Bragg spots of such a single crystallite do not necessarily fall onto the Ewald sphere; however, thermal diffuse scattering can be mapped in the given setup, peaking at the Bragg positions, and, with the small curvature of the Ewald sphere at high X-ray energies, mapping the symmetry of the reciprocal lattice [19]. Cooling below T_α gives rise to γ-reflections which are regularly arranged and well correlated with the α-orientations as seen in Fig. 13(c).

The residual α-pattern can be indexed as given in Fig. 13(b). By fortunate coincidence, the crystallite was aligned in a way such that we observe a plane in reciprocal space, spanned by the α-002 and α-200 reflections and with the α-$\bar{2}$20 normal. Slight inclination towards the beam favors the mapping of the upper right quadrant. The c-axis of the hexagonal lattice points to the upper right and the twofold symmetry of this orientation can be seen, expressed by a rectangular pattern.

The coarsening of the α-grains from 1344 to 1362 °C occurs in such a way that groups of many spots, around, for example, the α-002 position or the α-20$\bar{1}$ position, rearrange to form the new and large single spot. This may happen when two neighboring spots on the same ring stem from regions inclined by a small-angle boundary which has been broken up. However, neighboring spots may even merge together when they originally lie on different rings, i.e. neighboring grains have different crystallographic orientations by a large angle. For example, the
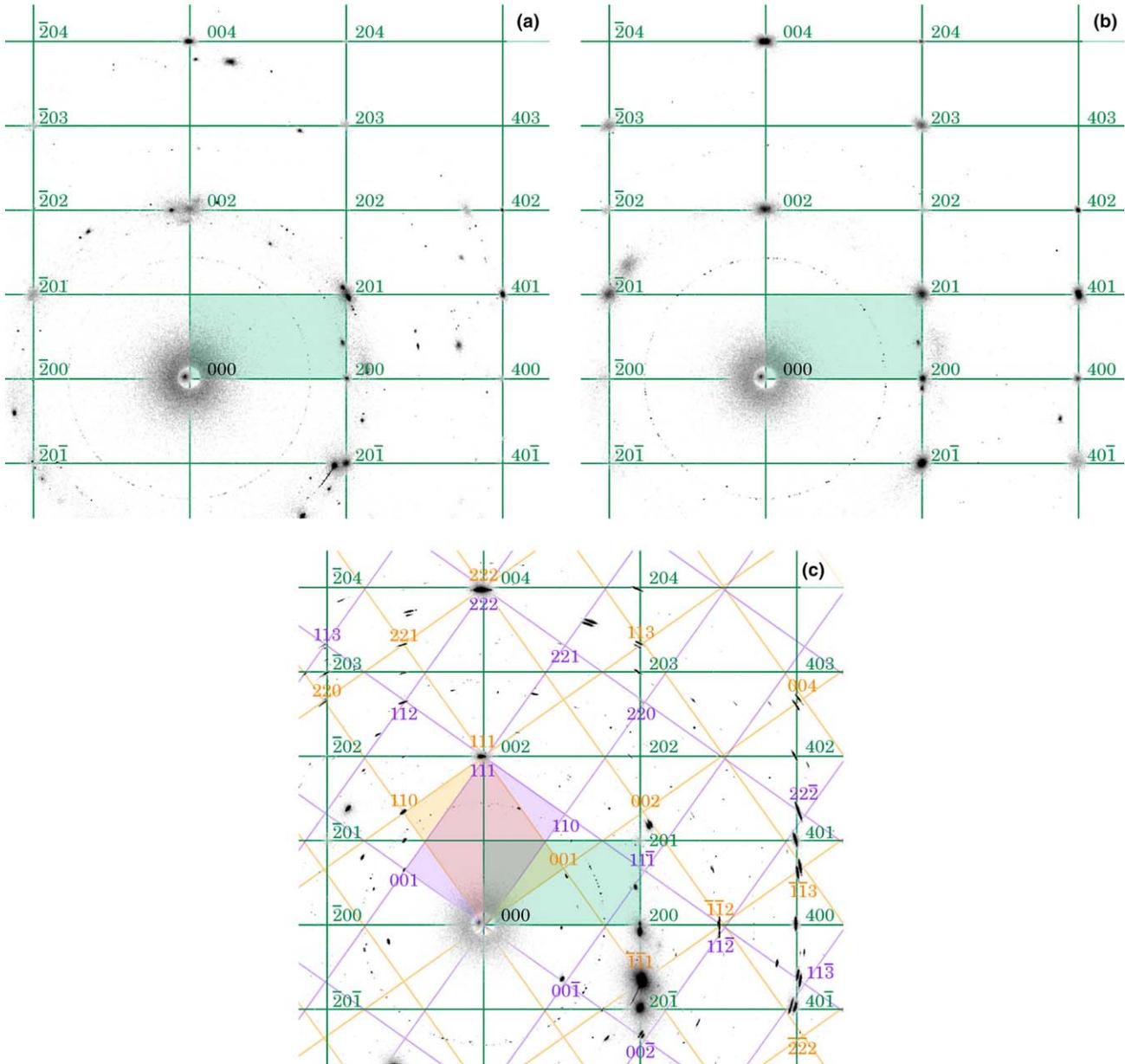
Fig. 13. (a) Diffraction patterns taken in situ from the α-phase at 1344 °C immediately after crossing the α + γ → α transition temperature, (b) 660 s later at 1362 °C, and (c) after re-entering and subsequent cooling to 1256 °C (Fig. 6). Data from (a) are identical to those of Fig. 8(f) after rotation of 30°. Grain growth takes place rapidly and a clear reciprocal lattice stemming from one large crystallite shows up in (b) which is shown by the green lines and indexed. The indication has been taken back to (a) and reveals reflections already grouping around these lattice positions, i.e. around 002, 201, and 20$\bar{1}$ reflections. In particular they show orientations of neighboring rings rearranging into the indexed reflections. The reappearance of the γ-phase in (c) is crystallographically well defined and reflections appear regularly between the α-reflections. They can be indexed by two separated γ-lattices drawn in orange and violet colors, coupled by a twin relationship and both sharing the γ-111 with the α-002 reflection. The γ-lattices further stake the $\overline{11}2$ with the twinned 11$\bar{2}$ reflections. The γ-indexing is given for a cubic approach of the tetragonal lattice and further splitting occurs due to three domain orientations of each twin orientation as observed for the orange 113 or $\overline{11}3$ reflections. Those distortions may relate in angular shifts and break up the coherence as indicated by the intensity lying between the γ-002 and α-201 positions which are governed by competing mechanisms.

lattice leading to a 201-type reflection may rearrange to a 002-type reflection. Both of these reflections correspond to lattice spacings which only differ by a few per cent, and the atoms have to rearrange only a little to swap the crystallographic orientation by a large angle, rather than to rotate the whole volume by this value. In addition, almost symmetric hexagons can be recognized in the rectangular diffraction pattern, such as the points (000, 201, 203, 004,

$\bar{2}$03, $\bar{2}$01), which are distorted by a few per cent only to match the hexagon of the basal plane. Such almost-twin relationships are another argument for correlated mechanism of grain growth.

The γ-phase and the α-phase after re-entering the α + γ-phase field are connected through the Blackburn relationship, in which α-002 and γ-111 fall together. As already discussed above, there exists an additional correlation

where the α-$\bar{2}20$ and, for example, the γ-$\bar{2}20$ reflections fall together. Then we can index the γ-$\overline{11}2$ spot which lies 90° to the γ-111 reflection and 3/4 to the α-400 vector. These two reciprocal lattice vectors span one plane in reciprocal space and many spots can be identified falling onto the rectangular pattern spanned by the reciprocal γ-001 and γ-110 vectors. Other spots can be identified by a second, simultaneously occurring reciprocal lattice, which is mirrored at the line from 000 to 111. It is the crystallographic twin with the common points $111 \rightarrow 111$ and $\overline{11}2 \rightarrow 11\bar{2}$.

All these considerations have been indexed with the notation for a cubic γ-lattice. The tetragonal lattice with lower symmetry gives rise to three different domains, depending in which cubic direction the c-axis is aligned. This expresses the splitting of reciprocal lattice spots, as discussed in Fig. 9, like the $00\bar{2}$ double spot on the first γ-lattice of Fig. 13(c), which at least stems from two domains. One kind of domain has the c-axis along $[100]$ or $[010]$ which is aligned to the $[001]$ direction of the other. Other clear domain splittings can be seen, for example, at the 113, $\overline{11}3$, and 004 spots of the twinned γ-lattice. As is known, domain formation leads always to small-angle boundaries, which, together with misfits to the symmetry of the α-structure, leads to mosaic-like spread. In plane, it amounts to 3° and should be similar to out of plane. Therefore, sharp reflections rather than diffuse spots as in the pure α-phase are observed, since the Ewald sphere is well cut within the width of the reflection determined by this mosaic distribution.

The reciprocal plane normal to the α-$\bar{2}20$ reflection can be described by three coherent reciprocal lattices, namely the α-lattice and the two twin γ-lattices. They correspond well to the observed microstructure of the IRE sample given in Fig. 5, which shows large grains made of coherent lamellae, i.e. regions with γ-laths of three domains and two twin orientations intersected by very fine α_2-lamellae.

4. Summary

High-energy synchrotron X-ray diffraction has been applied to characterize ex situ and in situ phase transitions, recrystallization behavior, and phase evolution in an intermetallic Ti–46Al–9Nb alloy. Debye–Scherrer rings, which are extremely rich in information, were recorded using a two-dimensional detector. Not only have variations of lattice parameters been evaluated as in standard powder diffraction techniques, but also the distribution of reflection spots spread along the azimuthal dimension of the rings. Continuous intensity distributions as attributed to fine grains can be distinguished from well-separated spots originating from coarse, individual grains. The comparison of diffraction patterns with micrographs obtained using optical and electron microscopy allows one to assign grain distributions to the coexisting phases, and this not only on different but also on superimposed Debye–Scherrer rings. Correlations of spots on different rings refer to coherences between different phases and domains. A $c/a \approx 1$ ratio was found in massively transformed material. This behavior is attributed both to internal stresses and chemical imbalance. Upon heating, at lower temperatures internal stresses first relax, while chemical separation onsets at 930 °C and continues increasingly rapidly when the α-transus temperature T_α is approached. Rapid grain growth is observed in the α-phase field making advantage of small atomic rearrangements which result in large changes of crystallographic orientation. Slow cooling below T_α leads to the reappearance of the γ-reflections, which are coherently aligned with two twin and all three domain orientations to the α-grain, showing the fully lamellar microstructure. The splitting of the α-002 from the γ-111 ring is observed upon heating, i.e. a large mismatch in the lattice parameters vanished after re-entrance into the phase mixture, which we attribute to more equilibrated chemical order in the second case since the system had time to relax.

References

[1] Kim Y-W, Clemens H, Rosenberger AH. Gamma titanium aluminides 2003. Warrendale (PA): TMS; 2003.
[2] Das G, Kestler H, Clemens H, Bartolotta PA. J Mater 2004;56:42–5.
[3] Kestler H, Clemens H. In: Peters M, Leyens C, editors. Titanium and titanium alloys. Weinheim, Germany: Wiley–VCH; 2003. p. 351–92.
[4] Appel F, Wagner R. Mater Sci Eng R 1998;22:187–268.
[5] Clemens H, Kestler H. Adv Eng Mater 2000;2:551–70.
[6] Bartels A, Kestler H, Clemens H. Mater Sci Eng A 2002:153–62.
[7] Sastry SML, Lipsitt HA. Metall Trans A 1977;8:1543–52.
[8] Yamaguchi M, Umakoshi Y. Prog Mater Sci 1990;34:1–148.
[9] Fujiwara T, Nakamura A, Hosomi M, Nishitani S, Shirai Y, Yamaguchi M. Philos Mag A 1990;61:591–606.
[10] Kishida K, Inui H, Yamaguchi M. Philos Mag A 1998;78:1–28.
[11] Paul JDH, Appel F, Wagner R. Acta Mater 1998;46:1075–85.
[12] Appel F, Brossmann U, Christoph U, Eggert S, Janschek P, Lorenz U, et al. Adv Eng Mater 2000;2:699–720.
[13] Aaronson HI, Vasudevan VK. Metall Mater Trans A 2002;33: 2445–70.
[14] Veeraraghavan D, Wang P, Vasudevan VK. Acta Mater 2003;51: 1721–41.
[15] Bartels A, Bystrzanowski S, Chladil H, Leitner H, Clemens H, Gerling R, et al. Mater Res Symp Proc 2005;842:S5.48.1.
[16] Clemens H, Bartels A, Bystrzanowski S, Chladil H, Leitner H, Dehm G, et al. Intermetallics 2006 [in press]. Available online 13 March 2006.
[17] Shull RD, Cline JP. High Temp Sci 1990;26:95–117.
[18] Novoselova T, Malinov S, Sha W, Zhecheva A. Mater Sci Eng A 2004;371:103–12.
[19] Liss K-D, Bartels A, Schreyer A, Clemens H. Textures Microstruct 2003;35:219–52.

[20] Gerling R, Bartels A, Clemens H, Kestler H, Schimansky F-P. Intermetallics 2004;12:275–80.

[21] Wang P, Veeraraghavan D, Kumar M, Vasudevan VK. Metall Mater Trans A 2002;33:2353–71.

[22] Wcislak L, Schneider JR, Tschentscher T, Klein H, Bunge HJ. Nucl Instrum Meth A 2001;467:1257–60.

[23] Poulsen HF, Nielsen SF, Lauridsen EM, Schmidt S, Suter RM, Lienert U, et al. J Appl Crystallogr 2001;34:751–6.

[24] Blackburn MJ. In: Jaffee RI, Promisel NE, editors. The science, technology and application of titanium alloys. New York (NY): Plenum Press; 1970. p. 633.

[25] Wolf W, Podloucky R. Unpublished data, 2005.